Rail to Digital automated up to autonomous train operation

D32.3 – ATO Impact On Infra-Structure

Assessment Analysis Report

Due date of deliverable: 30/11/2025

Actual submission date: 13/10/2025

Leader/Responsible of this Deliverable: Monique de Wit / ProRail

Reviewed: Y

Document status		
Revision	Date	Description
01	04/06/25	Document skeleton, chapters 1 to 4
02	04/08/25	First draft of document
03	15/08/25	Version for internal review
04	02/10/25	Updated version after internal review
05	13/10/25	Last updates, ready for TMT review
06	09/02/26	Updated version based on JU review
07	12/02/26	Updated version after internal review

Project funded from the European Union's Horizon Europe research and innovation programme		
Dissemination Level		
PU	Public	X
~~**SEN**~~	~~Sensitiv – limited under the conditions of the Grant Agreement~~	

Start date: 01/03/2023 Duration: 36 months

ACKNOWLEDGEMENTS

This project has received funding from the Europe's Rail Joint Undertaking (ERJU) under the Grant Agreement no. 101102001. The JU receives support from the European Union's Horizon Europe research and innovation programme and the Europe's Rail JU members other than the Union.

REPORT CONTRIBUTORS

Name	Company	Details of Contribution
Julian Hé	ProRail /TU Delft	Contributor
Zili Li	ProRail / TU Delft	Contributor
David Koopman	ProRail	Expert input / Reviewer
Emil Jansson	TRV / KTH	Reviewer
Thomas van den Berg	ProRail	Reviewer
Jesus Manuel Sanchez Dominguez	ADIF / Renfe	Reviewer
Monique de Wit	ProRail	Reviewer

EXECUTIVE SUMMARY

This report is a deliverable for the project R2DATO (FA2 WP32). Specifically, it is Deliverable 32.3, ATO Impact On Infra-Structure Assessment Analysis Report (Research on train infrastructure wear impact by applying ATO), Subtask 32.2.1: Analysis of the potential of infrastructure wear reduction (academic research), according to the Grant Agreement.

As an initial theoretical contribution, this work also develops a methodology that converts field test data into quantitative wear estimates. This framework links measured operational profiles to wheel–rail contact conditions and wear, providing a transferable basis for assessing infrastructure impact under different driving strategies.

To achieve this, field test data on train speed and traction torque were analysed to evaluate wheel–rail interaction. Multi-body dynamics simulations were used to derive slip ratios and contact forces, which were then combined with CONTACT program and established finite element models to estimate stresses, temperatures, and wear of rails. We applied a variant of Archard's wear law, calibrated with laboratory and field measurements, to compare ATO-induced wear with that of manual driving under similar conditions.

Based on the current data analysis, we find suggestive evidence that the ATO exhibits smoother torque and speed profiles, which, from the wear perspective, may result in an estimated 28% reduction in maintenance costs. It can significantly reduce wheel burns and wheel flats, thus reducing the dynamic loads on the infrastructure and rolling stock, as well as the noise and vibration nuisance.

The analysis has shown that ATO could already, in 2021, when the field tests were conducted, outperform manual driving. With the rapid development in control and especially AI technologies, it is reasonable to believe that future ATO can perform much better, contributing to a safe and cost-effective railway in general and infrastructure in particular.

The coefficient of friction (CoF) represents the adhesion level between the wheel and rail, defined as the ratio of the maximum transferable tangential force to the normal load in the contact patch. It is also clear that the coefficient of friction plays a critical role in avoiding wheel full slip, thus excessive wear and the consequential damage. It is therefore important for ATO trains to know in real-time the local CoF. This means that the development of technologies for real-time train-borne measurement of CoF is critically important for the success of ATO.

ABBREVIATIONS AND ACRONYMS

ATO	Automatic Train Operation
R2DATO	Rail to Digital automated up to autonomous train operation
ETCS	European Train Control System
GoA	Grade of Automation
RCF	Rolling Contact Fatigue
IJs	Insulated joints
ERTMS	European Rail Traffic Management System
S&Cs	Switches and Crossings
MBD	Multi-body Dynamics
3D	Three-dimensional
2D	Two-dimensional
FEM	Finite Element Models
FE	Finite Element
CoF	Coefficient of friction
OOR	Out of Roundness
WELs	White Etching Layers
ABA	Axle Box Acceleration
ADS	Adhesion Determination System
BAMS	Brake Adhesion Management System

TABLE OF CONTENTS

LIST OF FIGURES

LIST OF TABLES

1 INTRODUCTION

This report is a deliverable for the project Rail to Digital automated up to autonomous train operation (R2DATO) (FA2 WP32). Specifically, it is Deliverable 32.3, ATO (Automatic Train Operation) Impact On Infra-Structure Assessment Analysis Report (Research on train infrastructure wear impact by applying ATO), Subtask 32.2.1: Analysis of the potential of infrastructure wear reduction (academic research), according to the Grant Agreement.

The railway transportation system occupies a crucial role in contemporary transportation networks. Due to its safety, efficiency, and environmental benefits, railway transport has become an essential mode of transportation for numerous countries. The accelerating pace of urbanization and population growth has led to an increased demand for railway transport, resulting in higher train operation frequencies and speeds. In response to increasing demands for efficiency, reliability, and sustainability in modern railway operations, ATO systems have been implemented across various types of railway systems around the world. Since its early development in the 1960s [1], ATO has been tested and deployed in metro networks in major cities such as London, New York, Paris, Moscow, Stockholm, and Barcelona [2]. During the same period, ATO was also introduced on specialized main lines, including high-speed railways and freight corridors. Notable examples include early applications on the Tōkaidō Shinkansen in Japan [3] and the AutoHaul system in Australia, launched by Rio Tinto in 2018 as the world's first driverless heavy-haul long-distance rail operation [4].These implementations reflect the global interest and long-standing efforts to advance railway automation across different operational contexts.

This chapter first gives a brief overview of ATO trains Then, it shows that the focus of this report is the impact of ATO trains on wheel-rail wear and the rationale behind. Next, a review of the state of the art of the methods for analysing the wear is presented. The methods include wear models, Multi-body Dynamics (MBD), which are needed for computing the slip ratio, and the CONTACT software together with the Finite Element Model (FEM), which are needed for calculating the contact stress, flash temperature, and impact force related to wear.

1.1 ATO TRAINS

ATO trains operate under the coordinated control of two key systems: the ATO system and the European Train Control System (ETCS), as shown in Figure 1. These systems fulfil complementary roles in modern railway automation. ETCS functions as the train protection and signalling system, ensuring operational safety by supervising train speed, enforcing movement authority, and preventing collisions or derailments. By contrast, ATO is responsible for automating the train's driving tasks, including acceleration, cruising, coasting, and braking. While ETCS defines and monitors the operational boundaries to maintain safety, ATO optimizes train performance within those boundaries by delivering smooth and efficient motion. In addition, ETCS digitizes the communication between the interlocking and the train, whereas older Class-B train protection systems often require the driver to interpret signals. This digitalization enables the safe automation of the driving process.

The integration of ATO and ETCS enables higher levels of automation while upholding stringent safety standards, making the combination suitable for various railway applications, including metro, high-speed, and mainline systems. The effectiveness of an ATO system largely depends on its control algorithms, particularly those used to compute optimal speed profiles and regulate train movement through the precise application of tractive and braking forces.

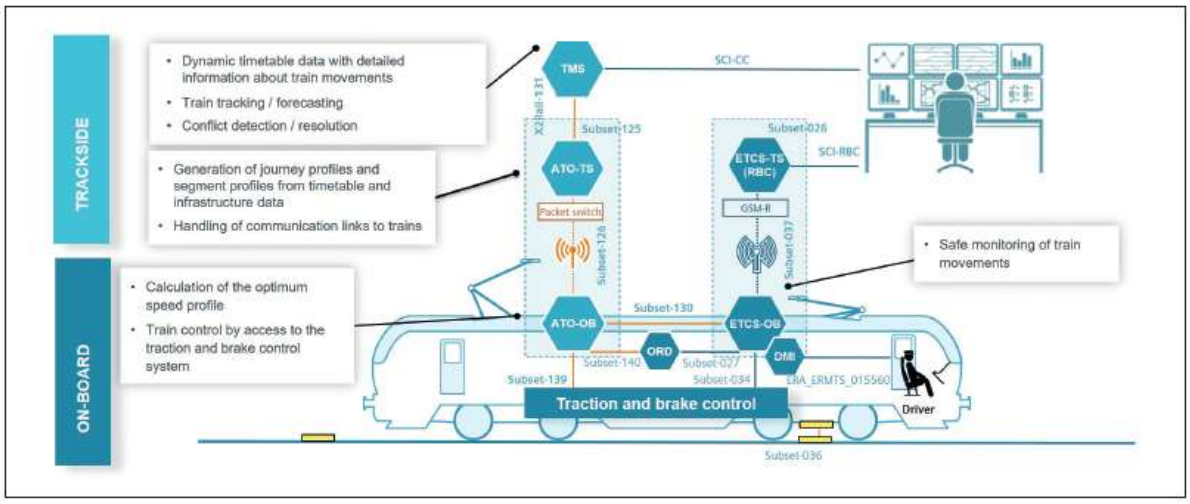

Figure 1:The control schematic of the ATO train [5]

Automation levels in ATO systems range from Grade of Automation (GoA)1 to GoA4 [2]. GoA 1 involves operations where a train driver manually controls the train. At GoA 2, the train's acceleration and braking are automated, but the driver remains on board. The driver focuses on tasks such as detecting obstructions, managing train dispatch, and initiating ATO. In GoA 3, known as "accompanied driverless operation," the train operates without a driver, though a train attendant is present to intervene in emergencies or handle any operational issues. All normal operations are fully automated. GoA 4 represents the highest level of automation, referred to as "unaccompanied driverless operation." There are no personnel on the train, and all functions are managed by technical systems or controlled remotely. In this report, the investigation is for the GoA 2 to GoA 4.

ATO, particularly at GoA 2 and higher, offers a broad range of operational, technical, and safety advantages. These benefits are not only applicable to semi-automated systems but also extend to fully driverless operations under GoA 3 and GoA 4. Many of the improvements attributed to ATO stem from its ability to control train speed profiles with high consistency and precision, as well as to enable more effective integration with modern traffic management strategies.

1.2 THE IMPACT OF THE ATO TRAINS ON INFRASTRUCTURE

The key function of an ATO system is “train speed control” (i.e., train driving), which is defined as the most important function for train operation in railways. On the one hand, its main aim is to ensure that operations remain within the boundaries defined by the safety system. On the other hand, ATO enables the speed control of trains as they travel along the track so that the jerk rates are within passenger comfort limits and the train speed is below the speed limit imposed by the safety system. The speed control function of ATO directly influences the railway infrastructure with the most pronounced effects occurring at the wheel–rail interface.

a) Limited Impact on Other Infrastructure

ATO systems mainly impact the tracks, especially at the wheel–rail interface. The wear on other already operating railway infrastructure components (such as power supply, communication, and signalling systems) is negligible. Although ATO could influence pantograph–catenary wear through operational profiles, the same wear mechanisms exist in conventional ETCS-supervised, driver-

operated services; therefore, this wear is not unique to ATO. Therefore, this study does not prioritize the wear of these components.

b) Acceptable Impact on Rolling Stock

ATO may have an impact on rolling stock, e.g., on braking discs, if rolling stock is considered as (part of the) infrastructure. If, however, the advantages of ATO for rolling stock weigh heavier than some limited and relatively minor disadvantages. For instance, the deployment of ATO adds rolling-stock-borne equipment—sensors, onboard processors, and interface modules—which entails incremental maintenance effort and recurrent costs for software updates, verification and validation (V&V), and safety certification. Nevertheless, given that ATO's benefits typically outweigh these limited drawbacks, the residual impact is generally considered acceptable. Therefore, we can accept these negative impacts as initial risks of technology implementation. Although we currently hypothesize a positive impact, this part of the study remains theoretical for now.

c) Wheel-Rail Interface

Under the influence of ATO systems, track wear primarily occurs at the wheel-rail contact interface, particularly at points of train acceleration and deceleration. ATO optimizes traction and braking actions, altering the distribution of longitudinal contact forces and directly impacting wheel-rail wear. Rolling Contact Fatigue (RCF), mainly squats, will be discussed as a consequence of the wear. The current research status and recommendations for further studies are provided in this report.

Compared to wear and RCF, plastic deformation is nowadays a less critical problem. Various types of corrugation, whose mechanisms remain unclear, require long-term research to evaluate ATO's impact. Additionally, ATO itself does not directly reduce the number of insulated joints (IJs). However, ATO is often deployed together with advanced signalling systems such as ETCS/ERTMS, where conventional track circuits are replaced by axle counters or jointless solutions. In such cases, the reliance on IJs decreases substantially, and therefore IJ degradation is considered outside the scope of this study. Finally, manually operated trains may contribute more to the degradation of switches and crossings (S&Cs). We will quantify and compare ATO-versus-manual impacts on S&C degradation in future work; this report does not analyse S&Cs. Therefore, this study focuses on evaluating the potential of ATO systems in reducing wheel-rail wear.

1.3 WEAR MODEL

To study how ATO affects rail wear, a quantitative method is needed to translate dynamic train-track interaction parameters such as slip ratio and contact force into material loss over time. Therefore, a wear model is required to link wheel–rail contact conditions with the resulting rail material removal by wear, enabling a realistic evaluation of operational impacts of ATO on rail. The wear of wheel and rail has been studied extensively. One typical wear model is listed in Table 1.

Table 1: Wear model

Wear models	Wear functions	Wear regimes	Notation
Archard [6]	Wear depth [m] $k\frac{Nd}{H}$		*k*: wear coefficient *N*: normal stress *H*: hardness *d*: the relative sliding distance

This model aim to predict wear depth, which is the thickness of material lost from a surface due to wear. Archard's wear model has been validated as reliable for predicting wheel-rail contact-induced wear [7, 8]. A variant of it will be employed in this study to predict wear development. The wear coefficient *k* will be identified from the measurements. It is evident that regardless of which wear model is used, the wheel and rail contact force and the relative sliding distance or velocity must be obtained to calculate the wear depth.

1.4 WHEEL AND RAIL INTERACTION MODELLING

1.4.1 Multi-body dynamics model

MBD modelling is a numerical method used to simulate the motion and interaction of interconnected rigid and flexible bodies. In railway studies, an MBD model can represent the train, track, and their dynamic contact behaviour under different operating conditions. It allows calculation of key parameters such as slip ratio, and contact forces, which can then be used as inputs, e.g., to FEMs, for further wear analysis. One significant advantage of MBD is its capability to simulate vehicle-track dynamics over long track sections. This makes MBD particularly suitable for studying the dynamic behaviour of trains in large-scale scenarios , e.g., for understanding the influence of such as slip ratios under different traction or braking conditions.

Numerous MBD models have been developed to investigate the formation and growth of wear on the wheel and rail interface. Morys [9] constructed a Three-dimensional (3D) MBD model of an ICE-1 carriage. Hertzian theory and FASTSIM [10] were used to calculate the normal and tangential contact solutions, respectively. To capture a broader range of dynamic behaviours and deformation patterns, M. Meywerk [11] developed an MBD model with a wheelset, where the wheel axle and rims were treated as flexible beams, and the bogie was simplified as a rigid frame. Kalker's linear theory [12] and Hertzian theory were employed to address the contact solutions. Andersson and Johanssons [13] developed a model incorporating multi-rigid body wheelsets and a bogie frame, as well as finite element rails. Hertzian theory and the Shen-Hedrick-Elkins model [14] were used for contact solutions. To address non-elliptical wheel-rail contact occurring in real-life operations [15], some MBD models applied non-Hertzian contact theories, such as ANALYN [16], modified Kik–Piotrowski [17], and FaStrip [18].

1.4.2 Finite element model

FEM is a numerical method that divides complex structures into smaller, simpler elements to calculate stresses, strains, and other physical responses under given loads and boundary conditions. In railway engineering, FEM can be used to analyse wheel–rail contact, track structures, and material behaviour under dynamic loads. It can also capture complex contact geometries, material elastic–plastic deformation, and thermo-mechanical coupling, making the contact calculations closer to real-world conditions. FEM complements MBD by providing detailed local stress and deformation information, which can be used for wear, fatigue, and damage predictions.

FEM enables accurate simulation of wheel–rail contact, particularly under non-Hertzian, thermo-mechanical, and elasto-plastic conditions. Zhao [19] presented a 3D transient finite element model with an elastic model to solve normal and tangential wheel-rail contact problems for arbitrary geometries using an explicit time integration scheme. This model, validated against Hertzian theory and Kalker's CONTACT software, effectively addresses high-frequency dynamic processes and examines the impact of element size on accuracy. Based on this method, a bilinear elasto-plastic material model was applied to obtain the contact solutions [20]. It explores plasticity effects on shear stress distribution and micro-slip. The model revealed that plastic flow alters the shape of the contact area and increases the interdependence of normal and tangential solutions, aiding in the understanding of wear mechanisms and crack initiation. Wei [21] presented a finite element model to study the evolution of frictional contact during non-stationary interactions, validated against classical half-space methods. Deng [22] developed a 3D transient finite element model to study the wheel and rail contact involving spin.

In addition, it has been found that the heat induced by wheel-rail frictional contact may significantly influence the material properties and consequently the evolution of wear [23]. Hence, friction-induced heat has been considered in some Finite Element (FE) contact models. Asih [23] developed a Two-dimensional (2D) FE model which applied an analytical moving heat flux on the rail to investigate the thermal effect on the wear rate of the rail. It was concluded that wear remains relatively small in the absence of wheelslip, whereas once wheelslip occurs it increases sharply, accompanied by contact temperatures exceeding 350 °C. Wu et al. [24] built a 2D FE rail model and applied an instantaneous heat source to analyse the thermal effect on the rail. They concluded that the thermal effect influences the residual stress, deformation, and plastic strain of the rail. Vo et al. [25] compared the wheel-rail contact temperatures calculated with a 2D model and a 3D model, and found that the peak temperature on the rail calculated with the 2D model was overestimated because the thermal energy emission in the transverse direction was overlooked.

However, besides the limitation of the Hertzian elastic assumption used in the moving heat sources, all the studies above prescribed the thermal effect in the wheel-rail contact load. In other words, the thermal effect that should be influenced by frictional contact were not updated in the simulations. To obtain more accurate contact solutions with the consideration of thermal effect, Naeimi et al. [26] proposed a 3D dynamic FE wheel-rail contact model that couples the mechanical and thermal load to investigate the stress-strain responses and flash temperature on the rail surface. Considering the temperature-dependent nonlinear material properties, the temperature and stress field in the contact area with a single wheel passage were obtained. The study concluded that the thermal softening of material induces higher von-Mises stresses and larger plastic deformation. The thermomechanical FE modeling approach proposed in [25] was then applied by Lian et al. [27] to study the fatigue life and wear behavior of a rail with multiple wheel loads. The thermomechanical FE model has been

applied to study the stress and the flash temperature of the corrugated rail [28]. A thermomechanical FE model has been developed and validated against experimental measurements, and this model has been applied to investigate the polygonal wear issues [29, 30].

In this study, we present the first attempt to incorporate field-measured traction and speed data into an MBD model to directly compare ATO-operated and manually operated trains in terms of wheel–rail contact behaviour and wear along the tracks. The output of the MBD simulations will then be input into Kalker's CONTACT and the thermomechanical FEM [26] to calculate the impact force, stress and micro-slip in the contact area, and the subsequent flash temperature. Finally, the contact solution will be applied to study the wheel and rail wear using Archard's wear model to assess the potential wear reduction of ATO trains. The main structure is shown in Figure 2.

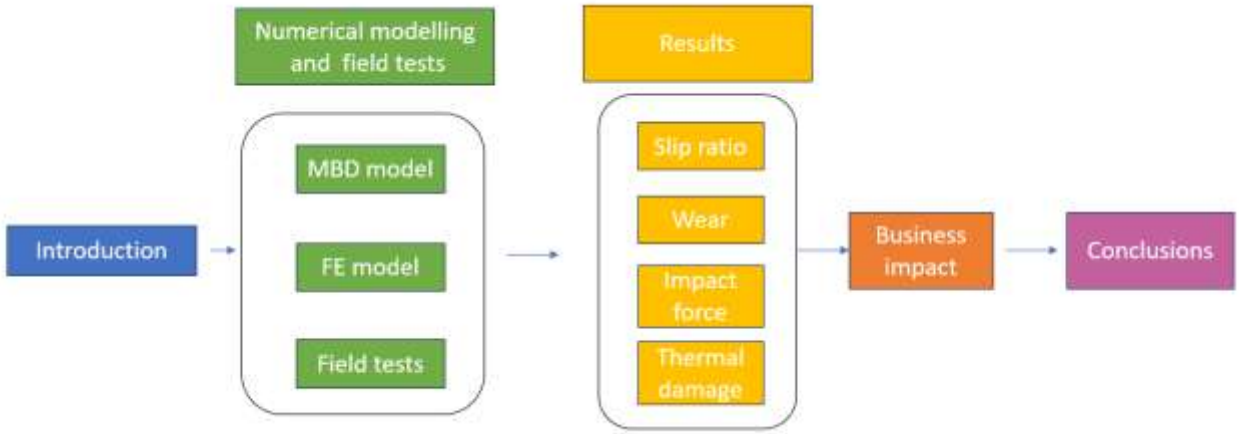

Figure 2: The main structure of investigation

The rest of this report is structured as follows. Section 2 introduces the numerical modelling framework and the field tests, including the MBD model, FE model, and the test programme. Section 3 presents the results in terms of slip ratio, wear, impact force, and thermal damage. Section 4 discusses the business impact of the findings, followed by the conclusions in Section 5.

2 THE NUMERICAL MODELS AND FIELD TEST

This chapter first introduces the numerical models used in the study, including the MBD model and the FEM. Field test data is then presented, which is used to compare the performance of ATO and manual operations in terms of wear and impact on railway infrastructure.

2.1 MULTI-BODY DYNAMICS (MBD) MODEL

The MBD model was developed using VI-Rail which is a commercial software [31] based on the GTW 2/8 train, a regional passenger train operating in the northern Netherlands and used in the field tests. Key specifications of the GTW 2/8 train are summarized in Table 2. Known from the field tests are the running speed as well as the tractive torque of the train over time with and without ATO functioning. The test was conducted with ATO GoA3.

Table 2 Parameters of the ATO train [32]

Series	GTW2/8
Length	56 m
Width	2.95 m
Height	4.3 m
Wheel radius	0.46 m
Weight	103 t
Top speed	140 km/h
Tractive effort	80 kN
Traction Power	600 ~ 1,100 kW

The GTW 2/8 train consists of four interconnected carriages, which are numbered 1 to 4 in Figure 3. The configuration includes a central power module and three passenger compartments. The power module is positioned between the two middle carriages, and is located under the second carriage. Since the slip ratios of the non-driving wheels in the rear carriages 3 and 4 are relatively low and have less impact on rail wear, they are not the focus of this study, and were not modelled in this study. Carriages 1 and 2 were combined into a single rigid body, assuming a straight-line operation and no relative motion. The mass and moment of inertia of this new carriage are recalculated based on the total length and weight of the carriages. The MBD model, illustrated in Figure 3, represents the rigid-body system of the train, incorporating essential components such as the bogies, suspension system, and wheel-rail interaction.

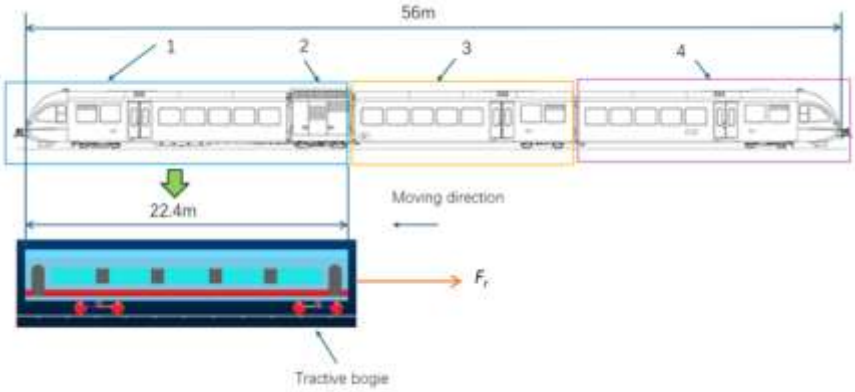

Figure 3: The MBD model of the GTW 2/8 train

The MBD model requires time-dependent tractive torque, resistance force and Coefficient of Friction (CoF) as inputs. In this model, the combined mass of the carbody and the two bogies was 53.251 t, accounting for 51.7% of the total train mass (103 t). Accordingly, the measured tractive torques were scaled by this proportion and then applied to the wheelsets in the MBD simulations. The tractive torques were recorded during the field tests with ATO (Case 1A,as shown in Figure 4. The occurrence of two distinct peaks in the train starting torque curve can be explained by several factors. During startup, the traction system output undergoes a rapid increase followed by a controlled adjustment phase, which causes multiple torque peaks. Dynamic variations in the wheel-rail friction conditions and slip ratio contribute to fluctuations in torque as well. In addition, control strategies applied by the ATO or the driver involve staged torque application to optimize acceleration. Mechanical inertia and the dynamic response of the drivetrain also affect the torque profile, leading to the observed double-peak characteristic. For each case, the measurements presented correspond to a single run. While this provides an initial insight into the system behaviour, it is acknowledged that driver variability could influence the results. Future studies may include multiple runs with different drivers to quantify this effect.

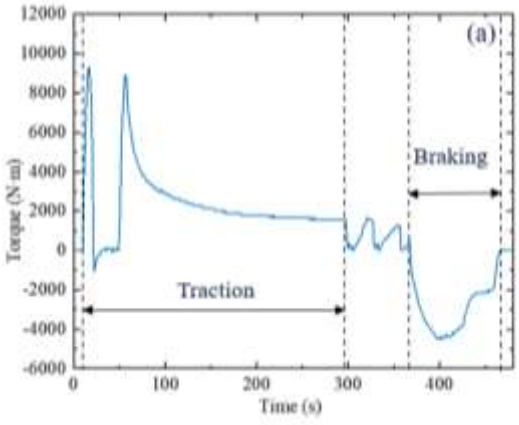

Figure 4: Tractive torque applied on the wheelset of ATO train

The measured speed curve was used to compute the resistance force, which was then applied to the carbody in the MBD simulations. Based on Newton's second law, the behaviour of the MBD model in Figure 3 can be described by the following equation:

$$T/R + F_r = m \times a \quad (1)$$

where *T* is the scaled tractive torque provided by the measurement (Figure 4), *R* is the wheel radius (0.46 m), F_r is the total resistance force acting on the train, m is the mass of the train (53.251 t), and a is the instantaneous acceleration. The instantaneous acceleration a can be obtained by differentiating the speed-time curve. Given that the speed variation follows:

$$v(t) = v_0 + at \quad (2)$$

where, $v(t)$ represents the speed at a given time t, v_0 is the initial speed at time zero. The acceleration at each time point can be calculated as the slope of the speed curve, i.e., the first derivative of speed with respect to time. In this study, both the speed-time curve and the tractive force-time curve are available from the experimental measurements (Figure 8 and 9). The total resistance force can therefore be determined at each time point by equation (1). Through this approach, the variation of the resistance forces over time was derived from the measured train speed and tractive force data.

The CoF between the wheel and rail was not measured during the tests. An estimation was made according to the weather conditions. According to [33], the limiting CoF for traction under humid conditions is 0.17. Under dry weather conditions, the CoF between the train and the track was measured to range from 0.24 to 0.42 in the UK using the Ontrak device [34]. Accordingly, a value of 0.35 is used as the dry CoF in this study.

2.2 Finite Element Model (FEM)

A 3D thermomechanical FE wheel-rail contact model was constructed [26] incorporating its geometrical, mechanical, and material characteristics, as depicted in Figure 5. This model is capable of replicating the motion of a wheel travelling along a track at a predefined slip ratio during traction and braking. The simulation procedure of the FE model includes four steps: 1. Modelling of wheel-rail contact (preprocessing in ANSYS); 2. Static equilibrium of the wheel loading on the rail (implicit integration in LS-DYNA); 3. Dynamic rolling of the wheel along the rail (explicit integration in LS-DYNA); 4. Results output and analysis (postprocessing with MATLAB).

The preprocessing of the FE modelling included geometry and material modelling, structural discretization, and the definitions of boundary conditions (including contact pairs), loads, and initial conditions. In terms of the geometry within the FE model, the track model spanned a total length of 8.75 metres, encompassing 14 sleeper spans, and included a 0.325-metre solution zone along the rail. The rail was fixed to the sleepers in three directions through fastenings. The sleepers were supported by the ballast and the subgrade. A wheel with a radius of 0.46 m and a half axle were modelled.

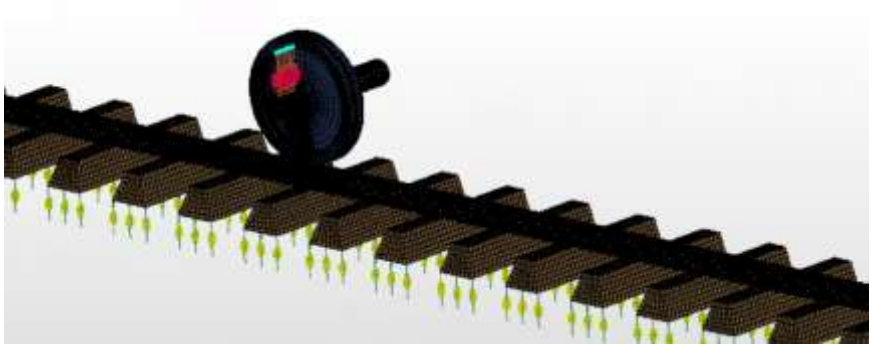

Figure 5:The thermomechanical finite element model

The wheel, rail, and sleepers were modelled with 8-node solid elements. The fastenings, ballast, and subgrade were modelled with spring-damper elements. To improve the calculation efficiency, a partly refined mesh strategy was applied. The finest mesh size of the top surface in the solution zone of the rail was 0.18 mm (x-axis) × 0.20 mm (y-axis) × 0.20 mm (z-axis). The FE model comprises 577,907 elements and 646,016 nodes. The minor axis of the contact area covers 13 contact elements; thus, sufficiently accurate contact solutions can be obtained for engineering applications [19].

2.3 FIELD TEST DATA OF ATO VS. MANUAL OPERATIONS

In this section, field test data are presented. First, four pairs of test cases are selected, each pair includes a test controlled by ATO and the other is manually controlled. Then the traction/braking torque and speed profiles are presented for each of the four pairs. Afterwards, it is shown how slip ratio is calculated from the torque and speed measurements. The slip ratio is needed for calculating the wear.

2.3.1 The field test cases

The field test data used in this study were collected from a series of tests conducted with a GTW2/8 train equipped with ATO [35]. The objective of this study is to evaluate the ATO system's capability to adhere to timetables, handle route variations and delays, and to assess its potential impact on energy consumption. The tests were conducted on the route from Buitenpost to Hoogkerk, with two intermediate station stops. In total, six test periods were carried out over 21 nights, resulting in 186 runs and approximately 3,800 km driven under ATO operation. From these, four representative cases were selected for detailed analysis in this report, each corresponding to a single test run. During the tests, the ATO system was either activated, or deactivated, enabling a comparative analysis of train speed and traction/braking force under automated and manual driving modes.

To investigate the differences in traction and braking performance between ATO and manual driving under varying operational conditions, a total of four pairs of cases are considered. These include four ATO-operated cases (Case 1A, 2A, 3A, 4A) and their corresponding manually driven counterparts (Case 1M, 2M, 3M, 4M). All manual runs were conducted by the same specially trained test driver. Consequently, the results may not reflect average operational driving and may have been influenced by the test environment and the fact that the driver was under evaluation.

These four pairs of cases were selected in this way: (1) It is preferred that each pair of an ATO and a manual test be performed on the same day. (2) If not on the same day, the weather of the two days should be comparable, and the maximum torque applied in the test should be comparable.

The four pairs of cases are by no means exhaustive/exclusive. The picture presented with the four pairs may be far from being complete. Broader and detailed research is needed. It also noted that the findings strongly depend on the ATO algorithm and its match with the hardware.

The CoF was assigned two distinct values, 0.17 and 0.35, to investigate the effects of different friction levels. The weather conditions, which are critical for the CoF, are summarized in Table 3.Due to varying weather conditions, such as fog and clear skies, slip behaviour was analyzed under both friction coefficients of 0.17 and 0.35 in the following sections.

Table 3: The weather conditions of the selected cases.

	Weather
Case 1A	Passing clouds
Case 1M	Fog
Case 2A	Over cast
Case 2M	Over cast
Case 3A	Passing clouds and Partly cloudy
Case 3M	Passing clouds
Case 4A	Clear
Case 4M	Clear

As shown in the table, all the cases took place on the same track section (Buitenpost to Hoogkerk), as shown in Figure 6. Although the actual track includes a curve (Figure 6), the straight track was considered in this study, avoiding the complexity of lateral force in curves.

Taking Cases 1A and 1M for example. The primary variation between the two cases lies in the time of operation: Case 1A took place on July 31, 2021, from 00:36 to 00:44, while Case 1M occurred on July 24, 2021, from 03:07 to 03:14. The coefficient of friction might vary between these days due to different weather conditions. Historical weather data were retrieved to determine the weather conditions during the tests, and the corresponding weather information is presented in Figure 7.

Figure 6:Track section for cases 1A and 1M (from openrailwaymap.app)

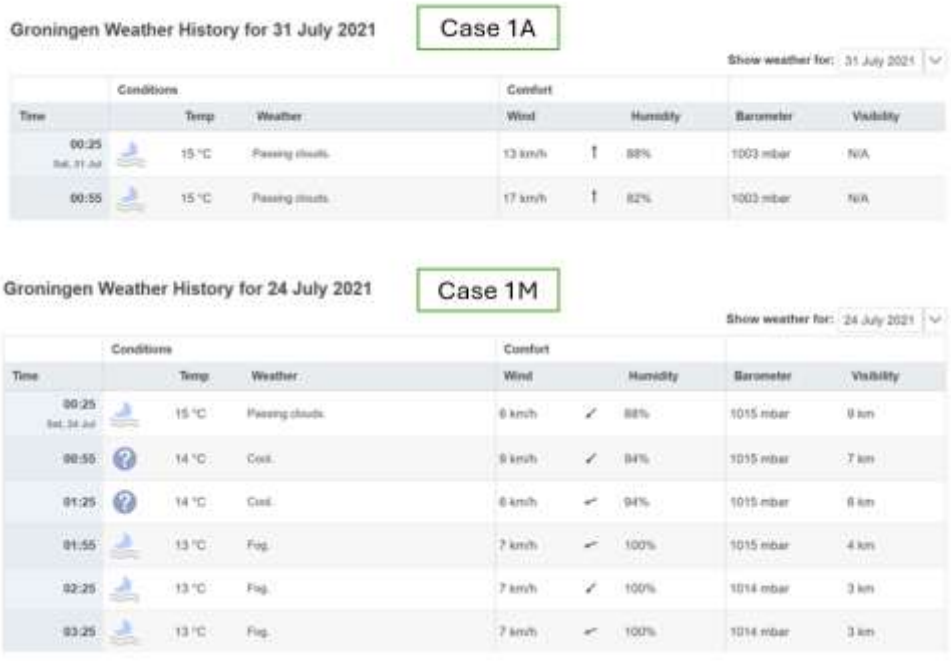

Figure 7: Weather conditions of Case 1A and Case 1M (from time and date website)

During the test of Case 1A, the weather was characterized by passing clouds with a relative humidity of 82 - 88%, suggesting that the rail surface could have been slightly wet. Case 1M was conducted under foggy conditions with 88 - 100% humidity, thus the rail could be wet. The same coefficient of friction, 0.17, which corresponds to a typical value under general wet conditions [33] was therefore used for both cases. Additionally, analyses were also performed using a higher coefficient of friction

of 0.35 to evaluate the effects of improved adhesion conditions. It should be noted that other contaminants, such as dust or lubricants, may influence the friction level; these effects, however, were not considered in the present analysis. Fallen leaves were also not included, as this section of railway mainly passes through agricultural fields where leaf contamination is limited. In addition, no comparative tests were conducted under rainy conditions, and a more detailed investigation can be carried out in future work.

The tractive torques were recorded during the field tests with ATO (Case 1A) and without ATO (Case 1M), as shown in Figure 8. . In both control modes, the torques increased from zero to nearly 10,000 N·m. The ATO control curve exhibits two distinct peaks in the traction phase, while the manual operation also shows two peaks, but with a shorter interval in between. In the braking phase, the torque under manual operation fluctuated significantly, whereas the torque curve under ATO control was smoother.

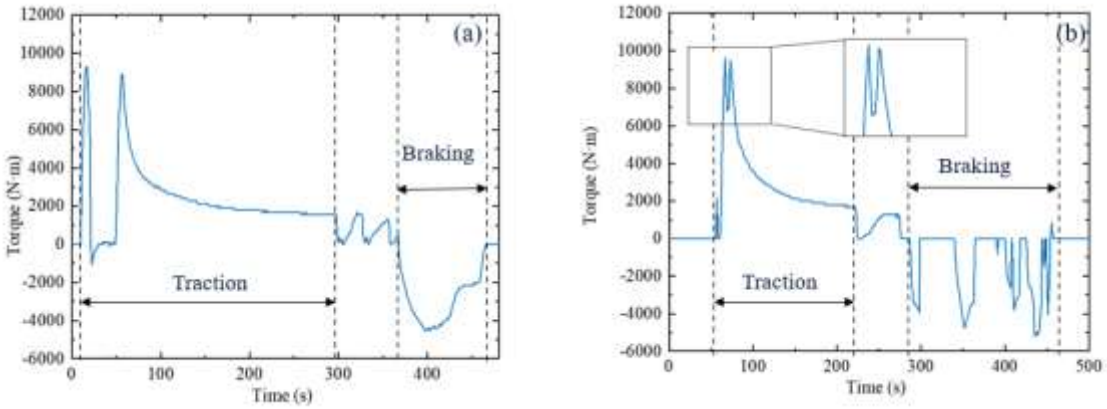

Figure 8: Tractive torque applied on the wheelset: (a) Case 1A; (b) Case 1M

Figure 9(a) shows that the speed profile of the ATO train is relatively smooth and includes a shorter cruising phase at peak speed. This indicates a well-regulated and controlled mode. In contrast, Figure 9(b) presents a case of faster acceleration followed by irregular deceleration with multiple abrupt drops in speed.

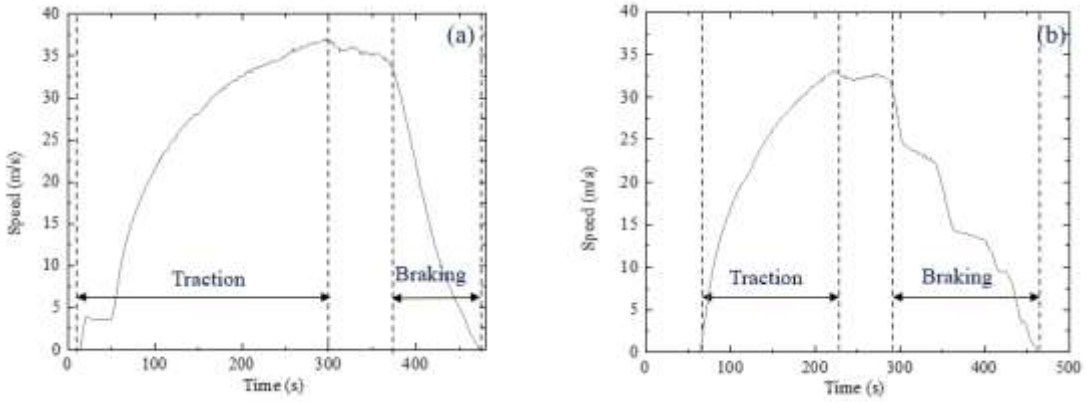

Figure 9: Measured longitudinal speed : (a) Case 1A; (b) Case 1M

Cases 2, 3, and 4 were selected as paired ATO and manual operations on the same train and routes within short time windows, enabling direct comparability of performance. Case 2 was tested under overcast conditions, with Case 2A representing an ATO run and Case 2M a manual run. Case 3 was conducted under passing clouds and fog, with both ATO and manual runs performed consecutively. Case 4 took place under clear and dry conditions, though additional simulations with a lower friction coefficient were conducted to represent wet tracks and to assess robustness against adverse conditions. Similar to Case 1A and 1M, the torque and speed curves from these three paired cases were used as input to the MBD model to calculate the slip ratio and contact forces.

2.3.2 Method for slip ratio calculation

By comparing the simulated speed and the measured speed, the reliability of the MBD model can be identified. The two speeds of the ATO train are shown in Figure 10.

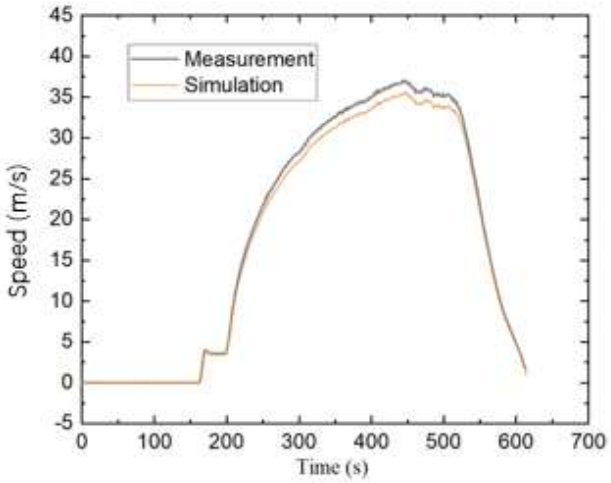

Figure 10: Comparison of the measured speed and the simulation speed (Case 1A)

As shown in Figure 10, the simulated train closely matches the measured velocity. The observed differences can be attributed to variations in train weight. The total train mass used in the simulation is 103 t, which is a nominal value; however, the actual weight during measurement may differ due to

the fuel load or the number of passengers on board. This parameter can be adjusted in future analyses.

The slip ratio is defined as the difference between the translational speed and the circumferential speed of the wheel divided by its translational speed. The translational and rotational speeds of the wheel can be obtained by the simulation. The slip ratio can be calculated using equation (3):

$$S = \frac{V-\omega R}{V} \times 100\% \quad (3)$$

where *S* denotes the slip ratio, V is the wheel translation velocity, and ω is the wheel rotational speed, *R* is the radius of the wheel.

3 RESULTS

In this section, results are presented using the models and data shown above. In Section 3.1, the slip ratios are obtained. Peak slip ratio is then identified and used in the wear model, which is derived from Archard's model in Section 3.2, to calculate the peak wear for cases 1A and 1M. To that end, wear coefficients are derived from field measurements and a laboratory test for partial and full slip cases. Large peak wear will cause wheel flats or wheel burns. The flats and burns will cause a large dynamic wheel-rail contact force. Section 3.3 shows, using data from a controlled laboratory test, that such a dynamic force can be 1.75 times the static contact force. Finally, Section 3.4 shows that under extreme operation conditions, peak slip ratio combined with high CoF, can cause flash temperature at wheel-rail contact that can cause material phase change, severe wear, and deformation.

3.1 PEAK SLIP RATIO CALCULATED WITH MBD

According to equation (3), the slip ratios over the entire period of cases 1A and 1M were calculated from the MBD simulations under wet and dry conditions. Although the tests were conducted under wet condition, a dry condition is also simulated to see the effect of CoF. Figure 11 presents the simulation results for the fourth wheelset—numbered from left to right—in the MBD model illustrated in Figure 3. As shown in Figure 11(a), two prominent peaks are observed in the slip ratio curves of ATO train around 14.31 s and 56.19 s, indicating traction scenarios during which the wheel-rail interface experiences peak slip. Under both CoF (0.17 for wet and 0.35 for dry contact), these peak slip ratios remain below 1%, suggesting that no wheel sliding occurred under ATO operation. The higher CoF results in the lower slip ratios, indicating an improved adhesion utilization.

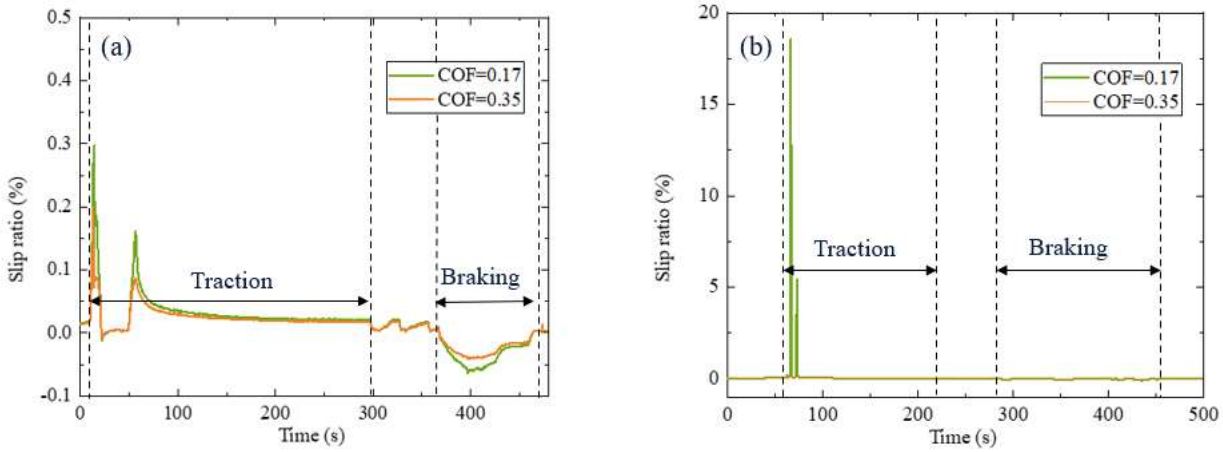

Figure 11: Slip ratios of the ATO-controlled train and the manually controlled train: (a) Case 1A; (b) Case 1M (Note that the Y-axis scales differ between the two plots, which should be considered when interpreting the contrast in slip ratio values.)

Table 4 summarizes the maximum slip ratio recorded under different traction conditions for both ATO-controlled and manually driven cases. Two friction conditions, represented by CoF of 0.17 and 0.35, were considered for each case. It can be observed that under the lower CoF of 0.17, the manually operated trains generally exhibited significantly higher maximum creepage values compared to their ATO counterparts, especially in Case 1M (18.3%), Case 2M (86%), and Case 3M (28%). This suggests that ATO control tends to provide smoother traction performance, effectively limiting excessive slip. However, an exception is found in Case 4A, where the ATO system showed a high creepage of 98%, which may suggest a control issue or poor running conditions in that particular run. This is the fundamental research on the potential wear of ATO train on the rail, the algorithm of the ATO system is unclear. Thus, the opposite trend of case 4 can be investigated in the future. Under the higher CoF of 0.35, the maximum creepage values remained low and relatively similar across all cases, typically below 0.4%, indicating stable contact conditions regardless of the control mode.

Table 4: Peak slip ratio (%) in the different cases, A and M mean ATO and Manual, respectively.

	CoF = 0.17		CoF = 0.35	
	A	M	A	M
Case 1	0.29	18.3	0.19	0.16
Case 2	22.00	86.00	0.12	0.32
Case 3	0.16	28.00	0.09	0.14
Case 4	98.00	0.19	0.09	0.09

3.2 WEAR AT PEAK SLIP RATIO

3.2.1 Method for wear calculation

Based on Archard's model in Table 1, i.e., equation. (4), a local wear model was developed in [36] and applied here to a contact area to compute the rail wear depth. The relationship between

Archard's wear and the local wear is given in equations (4) to (7). The wear depth of an element in the slip zone (see Figure 12) can be calculated by equation (7). Wear depth is defined as the reduction in surface material thickness caused by wear.

$$h_A = k\frac{Nd}{H} \tag{4}$$

$$h_{e(x,y)} = \frac{k}{H}P(x,y)\Delta d(x,y) \qquad (5)\Delta d(x,y) = s(x,y)\Delta t = V\xi(x,y)\frac{l}{V} = l\xi \tag{6}$$

$$h_{e(x,y)} = \frac{kl}{H}P(x,y)\xi \tag{7}$$

$$h_c = \frac{kl_{slipzone}}{H}P_{mean}\xi \tag{8}$$

where, h_A is the wear depth in the method of Archard. In Archard's model, the stress and slip distributions and thus the resulting wear are assumed to be uniform in the entire contact area. In wheel-rail contact, the stress and slip are non-uniform in the contact area. Archard's model, thus, when considering the wear of a rail, needs to be applied locally to each material "particle" of the rail to account for the stress and slip variations. A material particle is represented by an element in a numerical model. *k* is the wear coefficient, *N* is the normal stress, *d* is the relative sliding distance, and *H* is the hardness parameter.

$h_e(x,y)$ is the wear depth of an element at (x, y), $P(x,y)$ represents the normal stress distribution which can be obtained from a numerical model, $\Delta d(x,y)$ is the slip distance in an element and $s(x,y)$ is the corresponding slip velocity in the element. Δt is the time taken for the wheel to roll over one element, *V* is the translational velocity of the wheel, and *l* is the length of the element, as shown in Figure 11. ξ is the creepage.

In this study, *H* is converted from Vickers hardness [37].

$$H \approx 3\sigma_{UTS} \tag{9}$$

where, σ_{UTS} is the ultimate tensile strength, measured as 1022 MPa in [38]. Accordingly, the hardness parameter *H* is calculated to be 3066 MPa.

When the wheel rolls over a material particle of the rail surface, i.e., an element in the contact area of the rail, wear accumulates by adding up $h_e(x,y)$ of all the wear depth induced by all the elements in the wheel contact area that pass over the rail material particle. Equation (8) therefore defines the average wear depth h_c along the longitudinal axis of the contact area. $l_{slipzone}$ represents the length of the slip zone along the longitudinal axis, assuming the wheel moves through the contact patch at a constant speed. P_{mean} is the average normal stress along the longitudinal axis in the slip zone.

3.2.2 Wear coefficient for partial and full slip

In rolling contact, a contact area is divided into a slip area and an adhesion area, see Figure 12. When the adhesion area shrinks to zero, e.g., during wheel sliding, the contact is said to be in full slip. Otherwise, it is in partial slip.

The wear coefficient k_0 for the partial slip cases was estimated based on the field measurement on a straight track section near Steenwijk, the Netherlands [39]. Using equation (8), we calculated the wear coefficient k_0, as presented in equation(10).

$$k_0 = \frac{H\, h_{measured}}{l_{slipzone} P_{mean} \xi_c} \tag{10}$$

The value of k_0 is 0.01. Details about its determination is in [40]. This value will be used in the subsequent cases.

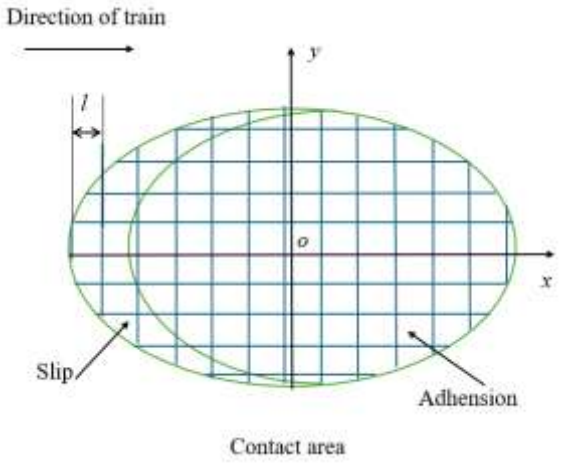

Figure 12: Discretization of contact area into elements

The wear coefficient under full slip conditions is determined based on measurements conducted using the V-Track test rig [41]. The experimental setup, including a thermal camera mounted on the rig, is illustrated in [41]. Details can be found in [40]

Based on equation (8), we calculated the wear coefficient k_1 in [41], as presented in equation (11).

$$k_1 = \frac{H\, C}{l_c P_{mean} \xi_c} \tag{11}$$

where, H = 3066 MPa), C is the measured wear depth, l_c is the length of longitudinal axis, P_{mean} is the average of normal stress along the longitudinal axis of the contact area within the slip zone, which is obtained by the FE model, and ξ_c is the slip ratio (40%). The value of k_1 is 0.77, and it is assumed to vary with the slip ratio, as higher slip ratios can lead to increased wear due to thermal effects. This value will be used in the subsequent cases, where the wear coefficient k_2 is 0.35 for the slip ratio 18.3% in Case 1M.

3.2.3 Peak wear depth in Cases 1A and 1M

Now the wear depth is calculated with CONTACT [42] for the peak slip ratios shown in Table 4. Take Case 1A for example, the peak slip ratios 0.29% takes place at 16.03s. Since it is partial slip, the wear coefficient is k_0 = 0.01, as is derived above.

The wear depth for Cases 1A and 1M is calculated in this way and shown in Table 4 for both CoF = 0.17 and 0.35. When the slip ratio is below 1%, the slip ratio is also called creepage, and the contact is in partial slip; k_0 = 0.01 is used. When the slip ratio is larger than 1%, k_2 = 0.35 is used for the wear coefficient.

Table 5: Wear depth along the longitudinal axis for the peak slip ratio in Case 1A and Case 1M, see Figure 10

CoF	ATO	manual operation
0.17	2.70×10^{-2} μm at 0.29% slip ratio	2.30×10^{2} μm at 18.3% slip ratio
0.35	3.50×10^{-3} μm at 0.19% slip ratio	2.90×10^{-3} μm at 0.16% slip ratio

As shown in Table 5, under low-CoF conditions (CoF = 0.17), the manually driven train generated significantly larger wear (2.30×10^{2} μm) compared to the ATO-operated train, which produced 2.70×10^{-2} μm of wear. This large difference is attributed to the high slip ratio and wheel sliding observed in Figure 10(b), which leads to severer wear conditions. Since these results reflect the wear of the rail caused by a single wheel pass, the continuous operation of trains under the manual driving mode would result in significant accumulation of rail wear over time. When the wear occurred on the wheel surface, a wheel flat with a depth of 0.2 mm could be a result.

In contrast, when the CoF was increased to 0.35, the total wear was reduced in both operation cases. The wear magnitudes under ATO and manual operation are comparable—3.50×10^{-3} μm and 2.90×10^{-3} μm, respectively. These findings emphasize the impact of driving strategy on wear behaviour, especially under low-CoF scenarios, and demonstrate the potential of ATO systems to reduce long-term rail degradation.

Based on equation (8), the wear depth is proportional to the slip ratio. Consequently, under low adhesion, the wear in Case 4A is expected to be much greater than in Case 4M. Under high adhesion, however, the wear depth remains low in both cases. It should be emphasized that this is a fundamental study focusing on the methodology. The specific ATO control algorithm is not known to us, and future research could be directed toward investigating how dedicated ATO algorithms may contribute to wear reduction. Nevertheless, the train showed good performance under dry conditions, suggesting that the available adhesion was sufficient. Therefore, measurement of the CoF is necessary to better understand the relationship between adhesion and train performance. The slip ratios of Table 4 were derived from four sets of test data. Analysis of more data is necessary to fully assess the performance of the ATO.

3.3 IMPACT FORCE CAUSED BY WHEEL FLATS

Impact loads are known to accelerate the degradation of track components by inducing high stress concentrations and localized damage. These loads are particularly pronounced when wheel defects, such as flats, are present [43].

Consider a wheel flat that is caused by an 18.3% slip ratio; the flat would have a depth of 0.23 mm, according to Table 5. Incorporating such a wheel flat into the FE model developed in [29], the dynamic interaction between the wheel and rail is analysed by varying the train speed.

The vertical dynamic contact force is presented in Figure 13. At a speed of 100 km/h, the presence of the wheel flat increases the peak wheel–rail contact force by 75%. The repetitive high-impact forces generated by wheel flats and the consequential wheel Out of Roundness (OOR) cause accelerated degradation of the track, such as damaged fastenings and sleepers, worn and fouled ballast. They generate air-borne noise and ground-borne vibrations, which are a nuisance to residents near railway tracks. On the wheel side, intensified impact stresses result in OOR wheel rolling contact fatigue, which can further cause components failure in rolling stock, like suspension system [44]. These effects result in not only reduced component life cycles and increased maintenance demands, but they can seriously compromised operational safety.

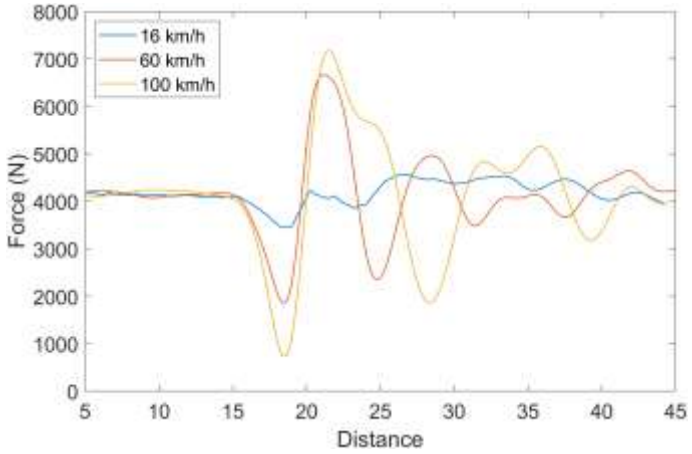

Figure 13: The effect of speeds on the impact force [43]

3.4 THERMAL DAMAGE ON THE RAIL SURFACE

Using the FE model of [26], the flash temperature of Case 1M is calculated for the peak slip ratio 18.3%. The flash temperature rise is 92 °C, shown in Table 6, together with the corresponding maximum contact pressure and current train speed.

In addition to Case 1M, a Case 5M was simulated with a higher slip ratio of 80% and a CoF of 0.45; these values are in the highest range that can occur in real-life railway operation, thus representing an extreme case. Such elevated slip ratios are likely to occur during emergency braking and under dry and clean wheel and rail contact. Under these conditions, intense sliding may develop at the contact interface, leading to substantial frictional heating and potentially severe thermomechanical effects such as surface damage or extreme wear.

Table 6: Cases of the FE model, with ambient temperature = 25 °C

Cases	Normal contact stress (GPa)	Running speed (m/s)	Slip ratio (%)	CoF	Temperature rise (°C)

Case 1M	1.06	1.83	18.3	0.17	92
Case 5M	1.06	1.83	80.0	0.45	812

It can be seen that the maximum flash temperature rise in Case 1M is 92 °C, which is not very high. This is because the slip ratio and CoF are not that high. In contrast, Case 5M results in a temperature rise of 812 °C, which is substantial enough to cause steel phase change, severe plastic deformation and wear due to thermal softening. Such rapid temperature rise followed by rapid cooling is believed to introduce high thermal stresses and promote the formation of White Etching Layers (WELs) in rail materials. WEL is reported to be a main cause of rolling contact fatigue of rails and wheels [45, 46]

4 BUSINESS IMPACT

Based on the analyses above, impact of ATO on infrastructure wear and degradation is shown with 3 cases: (1) Track maintenance costs by wear-induced squats; (2) Wheel burns on rails; (3) Wheel flats and the consequent wheel OOR, as well as their effects on track degradation and environmental noise and vibration. The consequences on rolling stock degradation, maintenance costs, and operation safety are also shown, though they are not considered here as railway “infrastructure”.

Table 4 shows that peak slip ratios take place when trains are not operated properly. Overall, ATO for a modern passenger train outperforms manual driving. It, however, needs further improvements, as in case 4A, it seems not to be sufficiently reliable. Table 5 shows that in extreme cases, very high flash temperature can cause wheel flats and wheel burns.

4.1 TRACK MAINTENANCE COSTS BY WEAR-INDUCED SQUATS

This case is about a monitored site of 200 m track near Weert, the Netherlands [47, 48]. The monitoring was between end of 2005 and end of 2008. At the beginning, the rail was just after maintenance grinding and no visible damage was present on the rail. At the end of the 3 years, the rails were with a lot of squats, see Figure 14 for an example.

Figure 14: A squat near Weert (NL)

Figure 15: shows that the squats are mostly between 25.9 – 26.1 km, i.e., at the end of the speed reduction. This shows a strong correlation with the train braking, implying that the squats were caused by a high slip ratio.

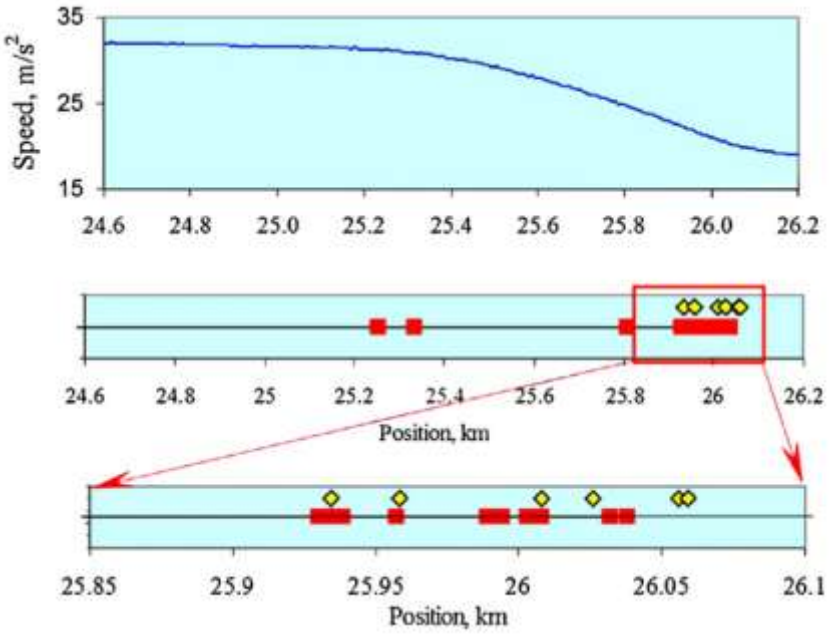

Figure 15: Upper drawing: a typical speed profile at the site. Middle and lower drawing: distribution of squats at the site. Train direction is from left to right. A red square indicates a severe squat, and a yellow diamond indicates a moderate squat. [47]

In [49], the relationship between the actual maintenance cost and different track damage mechanisms is represented by a multi-variable logarithmic regression model:

$$C_{actual} = KD_1^b D_2^c D_3^d \tag{12}$$

Where C_{actual} is the estimated maintenance cost per unit length of track, and $D_1, D_2,$ and D_3 denote the damage indices associated with wear, RCF, and track geometry degradation, respectively, which can be obtained by the modelling simulation. The coefficient *K* represents a scaling constant derived from empirical data, while the exponents *b, c*, and *d* quantify the relative contribution of each damage mechanism to the overall cost. These constant factors can be obtained by the cost of the practical maintenance case.

This formulation captures the nonlinear relationship between physical degradation and maintenance expenditure, allowing engineering-based damage models to be coupled with economic assessments. Based on the simulation results in Table 5, the manual-to-ATO slip ratio (e.g. $R_S = 18.3\%/0.29\%$) and corresponding wear ratio (e.g. R_w =230/ 0.027) can be calculated, as listed in Table 7. It should be noted that the relative wear for Case 1 is obtained under the condition of CoF = 0.17, as shown in Table 5. Assuming the same relationship between the relative slip ratio and relative wear, the relative wear ratios for the other cases can be derived from the slip ratio ratios listed in Table 4.

Table 7: Comparison of relative slip ratio and relative wear ratio between manual and ATO operations (CoF=0.17)

Case	Relative slip ratio ($R_S = S_M/S_A$)	Relative wear ($R_w = W_M/W_A$)
1	63.0	8.52×10^3
2	3.91	1.95×10^1
3	175	7.76×10^4
4	0.00194	1.23×10^{-6}

Based on equation (12), the present analysis focuses solely on the effect of wear (D_1) on the maintenance cost estimation. Other potential contributors to track deterioration, such as RCF and geometric degradation, are beyond the current scope.

The relationship between maintenance cost and wear magnitude can be expressed as a power-law function as mentioned in equation (12).

$$C \propto D_1^b \tag{13}$$

where *C* is the maintenance cost, D_1 represents the wear-related damage indicator, the median value of the relative wear ($R_w = 4270$) between manual and ATO operations is used in this analysis. *b* is the cost sensitivity coefficient that describes how strongly maintenance cost responds to wear. Since no actual track maintenance cost data are available, the cost sensitivity coefficient *b* is assumed to be 0.04 [49] . Thus, the relative maintenance cost can be obtained by equation (14).

$$\frac{C_{Manual}}{C_{ATO}} = (R_w)^b \tag{14}$$

where C_{manual} is the track maintenance cost caused by the manual operated train, C_{ATO} is the track maintenance cost caused by the ATO train. Based on the current data analysis, the maintenance cost under manual operation is approximately 1.4 times as high as that under ATO operation. This difference, when considered solely from the wear perspective, implies an estimated 28% reduction in maintenance costs for ATO-controlled operation. This is based only on 4 cases. A limitation of this study is that the wider traffic context and detailed ATO driving strategies were not analysed. For example, ATO may apply braking more consistently at the same locations compared with manual driving, which could have implications for localised wear. Such aspects require further investigation in future work. Much more extensive study is needed for a reliable conclusion.

With development in control and AI technology, it is reasonable to believe that ATO control algorithm can be significantly improved, meaning its effect on rail maintenance costs can be further increased. Rail maintenance costs consist of a large part of the track maintenance costs.

4.2 WHEEL BURNS ON RAILS

Table 5 shows that manual operation may cause a wheel flat of 0.23 mm deep. Figure 16 shows 2 wheel burns caused by spinning wheels and Figure 17 shows a wheel burn by a braking wheel. Wheel burns develop into squats, which are the major rail rolling contact problem worldwide. They threaten train operation safety because of the danger of a rail break.

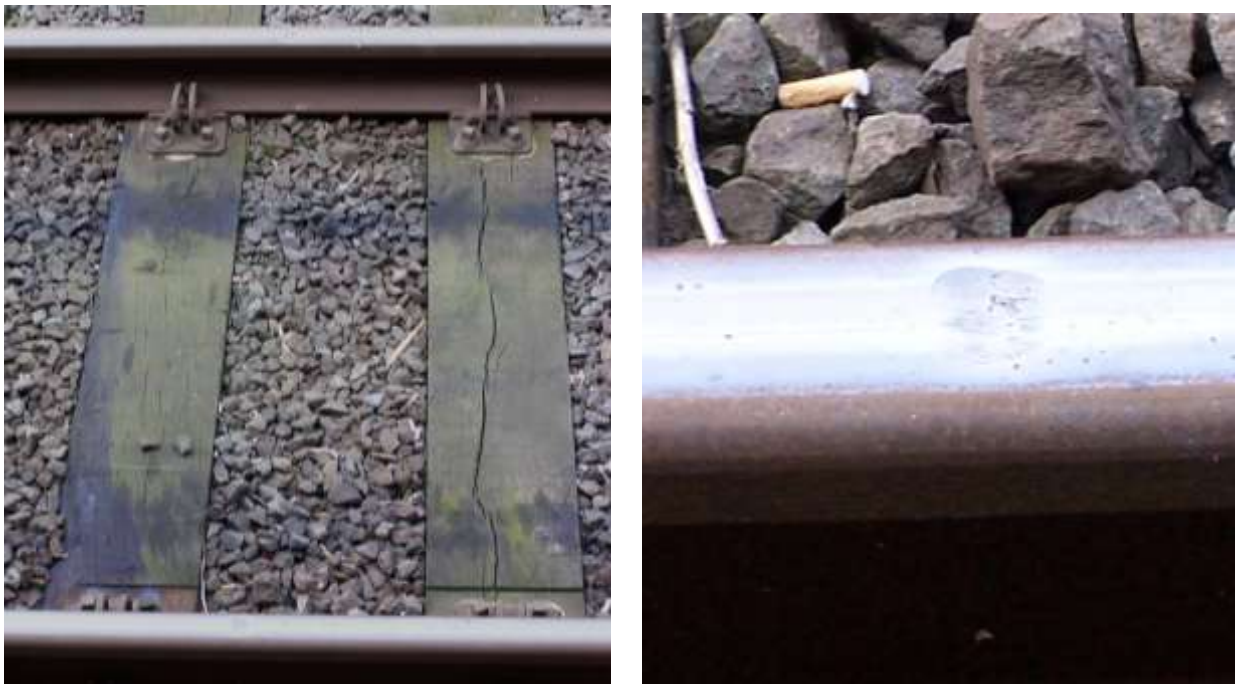

Figure 16: (a) A pair of wheel burns and (b) the wheel burn of the lower rail in (a). These kind of wheel burns are caused by spinning wheels when trains starts up where the CoF is low. The wheel burns were evolving into severe squats.

Figure 17: A wheel burn caused by a skidding wheel during braking

As Table 4 and 5 shows, ATO can reduce wheel burns, thus help reduce maintenance costs and improve operation safety.

4.3 WHEEL FLATS AND THE CONSEQUENT WHEEL OUT-OF-ROUNDNESS (OOR)

When the peak local wear happens on wheels, it is wheel flats. Figure 18 shows rolling contact fatigue caused by a wheel flats. Wheel flats are a major cause of wheel polygonization. Figure 19 shows examples of wheel polygons.

Wheel flats and polygons are together called wheel OOR. OOR has the following consequences:

(1) They will develop into rolling contact fatigue in wheels, potentially causing wheel failure, endangering train safety.
(2) They cause repeated impact between wheel and rail, cause noise and vibration, as well as accelerated degradation of track components and structures, such as broken fastening, cracked sleepers and worn ballast. Figure 20 (f) shows a broken clip of rail fastener. The noise and vibration are a nuisance to the residents along railway tracks. Statistics show that OOR is the most important train-maintenance-related factor that causes complaints about train-induced ground vibration [50].
(3) The impact causes damage to rolling stock, as shown in Figure 20 (a-e).

Figure 18: Wheel rolling contact caused by a wheel flat

Figure 19: Wheel polygon in a metro [51](used under CC BY 4.0 cropped from original)

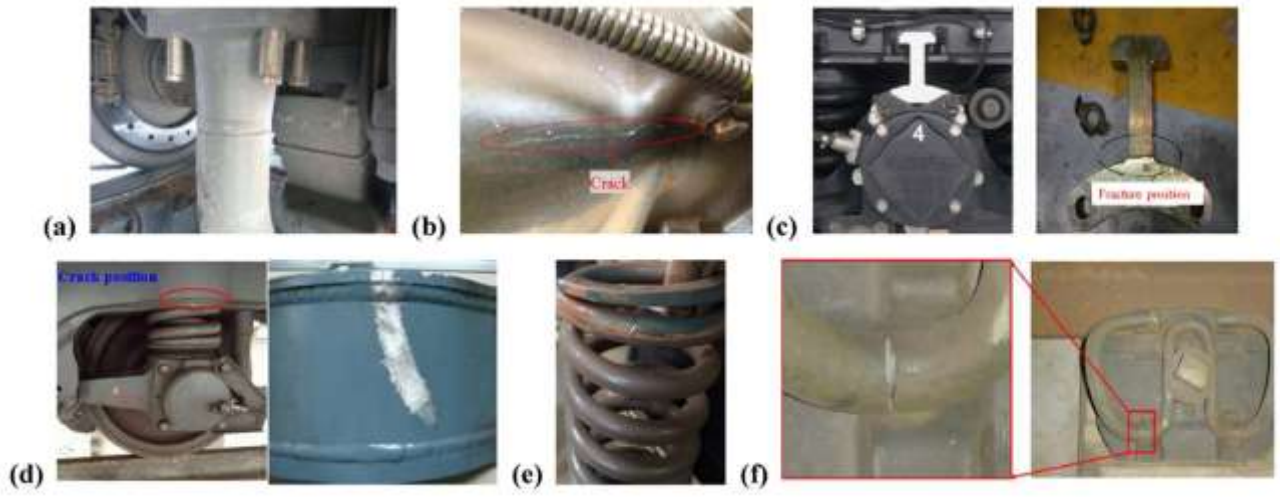

Figure 20: Damage to rolling stock and track caused by wheel polygon, (a) a supporting tube of the sanding device; (b) cracks of the gearbox; (c) cracks of the axle box; (d) cracks of the bogie frame; (e) cracks of the steel coil spring; (f) cracks of the rail fastener [51] (used under CC BY 4.0 cropped from original)

To combat the train-induced wear and damage: for rail, it is necessary to detect earlier by, e.g., Axle Box Acceleration(ABA) and maintain by, e.g., grinding, in time. For wheels, the OOR can be detected by Quo-Vadis and then machining the wheels in time. All these add up to maintenance and operation costs. It is therefore best to avoid, or at least minimise the train-induced wear and damage, by improving ATO algorithm.

5 DISCUSSION

The analysis has been done by comparing ATO with manual operation for 4 cases under the same COFs: 0.17 for wet and 0.35 for dry conditions. The ATO performance is generally better, with smoother speed profiles and fewer wheel-sliding incidents. It would be interesting to vary the COF to see if the better performance of ATO holds for other COF values, and if not, how ATO can be improved by 'learning' from humans by way of, e.g., AI. The performance of an ATO depends on its control algorithm and its electromechanical system. Better performance of one ATO type does not guarantee better performance of another. It is important to verify and optimise the performance of each type across the entire range of COF for the intended operating conditions.

Physics dictates that no matter how capable an ATO is, its traction and braking capacity are limited by the available COF at a given moment and location, for instance, during the leaf-falling season. In general, COF can vary greatly from time to time and place to place. Real-time COF estimation,

combined with friction management, is therefore necessary to minimise the sensitivity and uncertainties, and to realise the full potential of ATO.

Wear coefficients have been used to show the detrimental effect of full wheel slip. The coefficients were determined from field data for partial slip and a laboratory test for full slip. While the coefficient for partial slip is mainly determined by abrasion, the coefficient for full slip depends on the slip ratio. At higher slip ratios, the flash temperature at the wheel-rail contact is elevated, softening the material, causing material phase change, plastic deformation, and even melting, leading to severe local wear. It is therefore important to determine the threshold slip ratio, below which no significant damage is induced to the rail infrastructure. Such a threshold can be used as an objective in optimising the ATO control algorithm.

The cost exponent used is from the literature for a comparative study. The actual value for the Dutch railway used in the case study is missing. In general, research on the quantitative relationships between actual maintenance costs and different track-damage mechanisms is highly desired but challenging.

To extend the evidence base on how ATO performs relative to human drivers, it is interesting to compare more types of ATO trains with more human drivers, covering the full COF range under intended operating conditions. It would also be necessary to compare the performance on curved tracks.

Nevertheless, technological advancements in motor and vehicle design, power electronics, sensing, control, and AI continue to shape the assessment of how ATO performance compares with human drivers. A comparable example is the recent advancements in autonomous driving in the automotive industry. To realise the full potential of ATO, one of the most important research and development efforts is real-time COF estimation, which links to the investigations on the Adhesion Determination System and the Brake Adhesion Management System in R2DATO WP17 and 18 and IAM4RAIL WP5 and 6 Adhesion estimation for management

6 CONCLUSIONS AND RECOMMENDATIONS FOR NEXT STEP

6.1 CONCLUSIONS

This study evaluated the impact of the ATO system on rail wear by simulating two groups of real-life operating cases—one with and the other without ATO—on the same track under similar environmental conditions. Using measured train speed and wheel torque data, MBD train-track interaction simulations were performed to obtain wheel-rail contact forces and slip ratios. The normal contact stress and the microslip were then calculated by using CONTACT program as input parameters for wear calculation. Rail wear was then quantified using a modified Archard's wear model based on the MBD simulation and contact calculation results.

The following conclusions can be drawn:

1) This study presents a practical methodology for evaluating rail wear induced by trains with specific traction/braking control strategies by integrating measurement data (wheel torque and train speed profile) with MBD simulations. This approach can be extended to assess the impacts of other operational strategies, vehicle types, or infrastructure conditions on wheel-rail contact behaviour and interface deteriorations.

2) The ATO has the potential to avoid wheel sliding and thus reduce the wear. In 3 of the 4 studied cases, the peak rail wear under ATO operation is much lower than that under manual driving when the CoF is 0.17. This can be attributed to the more stable traction/ braking behaviour of ATO. Caution should, of course, be exercised because the study considered only 4 cases and much more extensive investigation is still needed.

3) Preliminary findings suggest that ATO may help mitigate peak slip wear, squats, wheel burns, wheel flats, and rail fastener breakage.

4) Preliminary results indicate that ATO operation has the potential to reduce wheel–rail damage costs by around 28%, though further validation is needed.

5) Wheel-sliding induced by manual operation can significantly increase rail wear. Implementing driver assistance (e.g. Driver Advisory System [5, 16]) can mitigate traction- and braking-related wear by encouraging smoother driving; however, their effect depends on driver compliance and lacks the closed-loop enforcement of ATO. They are therefore a complement, not a substitute for ATO.

6.2 RECOMMENDATIONS FOR NEXT STEPS

It is also clear from Tables 4, 5, and 6 that the CoF plays a critical role in avoiding wheel full slip, thus excessive wear and the consequential damage. It is therefore important for ATO trains to know in real-time the local CoF. This means that the development of technologies for real-time train-borne measurement of CoF is critically important for the success of ATO. This links to R2DATO Work package 17 and 18: New-generation braking systems, where investigations on the Adhesion Determination System (ADS) and the Brake Adhesion Management System (BAMS) are carried out. The results of this work are shared with R2DATO WP17 and WP18. Moreover, this could also be useful for IAM4RAIL WP5 and 6.

The analysis shows, based on 4 cases, that ATO could already, in 2021, when the field tests were conducted, outperform manual driving. If this finding holds generally, and if assessment of CoF in real time becomes available, it is reasonable to believe that, with the rapid development in control and especially AI technologies, future ATO can perform much better [52, 53], contributing to safe and cost-effective railway in general and infrastructure in particular.

Degradation of switches and crossings (S&Cs) is highly sensitive to dynamic impact loads and variability in approach speed and braking; any increase in impact severity or creepage energy accelerates wear, rolling-contact fatigue, and plastic flow. Accordingly, compared with a smooth, rule-compliant ATO profile, the greater variance typical of manual driving may be more detrimental. We can quantify the ATO-versus-manual effect in subsequent work using site measurements and turnout-damage modelling.

REFERENCES [1 – 53]

[1] R. Dell, A.W. Manse, Automatic driving of passenger trains on London Transport, Proc Inst Mech Eng 179(3A) (1964) 24–38.
[2] J.P. Powell, A. Fraszczyk, C.N. Cheong, H.K. Yeung, Potential Benefits and Obstacles of Implementing Driverless Train Operation on the Tyne and Wear Metro: A Simulation Exercise, Urban Rail Transit, 2 (2016) 114-127.
[3] T. Ito, H. Ebihara, Automatic train operation by programme control, Proc Inst Mech Eng 179(3A) (1964) 57–61.
[4] M. M. Yusuf, A., Stuart, R., & Miyazaki, H. ,, Heavy haul freight transportation system: AutoHaul—Autonomous heavy haul freight train achieved in Australia, Hitachi Rev, ,, 69(6), 790-791 (2020).
[5] J. Yin, T. Tang, L. Yang, J. Xun, Y. Huang, Z. Gao, Research and development of automatic train operation for railway transportation systems: A survey, Transportation Research Part C: Emerging Technologies, 85 (2017) 548-572.
[6] J.F. Archard, Contact and Rubbing of Flat Surfaces, Journal of Applied Physics, 24 (1953) 981-988.
[7] T. Jendel, Prediction of wheel profile wear—comparisons with field measurements, Wear, 253 (2002) 89-99.
[8] J. Brouzoulis, P.T. Torstensson, R. Stock, M. Ekh, Prediction of wear and plastic flow in rails—Test rig results, model calibration and numerical prediction, Wear, 271 (2011) 92-99.
[9] B. Morys, Enlargement of out-of-round wheel profiles on high speed trains, Journal of Sound and Vibration, 227 (1999) 965-978.
[10] J.J. Kalker, A fast algorithm for the simplified theory of rolling contact, Vehicle System Dynamics, 11 (2007) 1-13.
[11] M. Meywerk, Polygonalization of railway wheels, Archive of Applied Mechanics, 69 (1999) 105-120.
[12] J.J. Kalker, Survey of wheel—rail rolling contact theory, Vehicle System Dynamics, 8 (2007) 317-358.
[13] C. Andersson, A. Johansson, Prediction of rail corrugation generated by three-dimensional wheel–rail interaction, Wear, 257 (2004) 423-434.
[14] Z. Shen, J. Hedrick, J. Elkins, A comparison of alternative creep force models for rail vehicle dynamic analysis, Vehicle System Dynamics, 12 (2007) 79-83.
[15] N. Burgelman, M.S. Sichani, R. Enblom, M. Berg, Z. Li, R. Dollevoet, Influence of wheel–rail contact modelling on vehicle dynamic simulation, Vehicle System Dynamics, 53 (2015) 1190-1203.
[16] M. Sh. Sichani, R. Enblom, M. Berg, A novel method to model wheel–rail normal contact in vehicle dynamics simulation, Vehicle System Dynamics, 52 (2014) 1752-1764.
[17] Y. Sun, W. Zhai, Y. Guo, A robust non-Hertzian contact method for wheel–rail normal contact analysis, Vehicle System Dynamics, 56 (2018) 1899-1921.
[18] M. Sh. Sichani, R. Enblom, M. Berg, An alternative to FASTSIM for tangential solution of the wheel–rail contact, Vehicle System Dynamics, (2016) 748-764.
[19] X. Zhao, Z. Li, The solution of frictional wheel–rail rolling contact with a 3D transient finite element model: Validation and error analysis, Wear, 271 (2011) 444-452.
[20] X. Zhao, Z. Li, A three-dimensional finite element solution of frictional wheel–rail rolling contact in elasto-plasticity, Proceedings of the Institution of Mechanical Engineers, Part J: Journal of Engineering Tribology, 229 (2015) 86-100.
[21] Z. Wei, Z. Li, Z. Qian, R. Chen, R. Dollevoet, 3D FE modelling and validation of frictional contact with partial slip in compression–shift–rolling evolution, International Journal of Rail Transportation, 4 (2015) 20-36.
[22] X. Deng, Z. Qian, R.J.J.o.T. Dollevoet, Lagrangian explicit finite element modeling for spin-rolling contact, 137 (2015) 041401.
[23] A.M.S. Asih, K. Ding, A. Kapoor, Modelling rail wear transition and mechanism due to frictional heating, Wear, 284-285 (2012) 82-90.

[24] L. Wu, Z. Wen, W. Li, X. Jin, Thermo-elastic–plastic finite element analysis of wheel/rail sliding contact, Wear, 271 (2011) 437-443.
[25] K. Vo, A.K. Tieu, H. Zhu, P. Kosasih, The influence of high temperature due to high adhesion condition on rail damage, Wear, 330 (2015) 571-580.
[26] M. Naeimi, S. Li, Z. Li, J. Wu, R.H. Petrov, J. Sietsma, R. Dollevoet, Thermomechanical analysis of the wheel-rail contact using a coupled modelling procedure, Tribology International, 117 (2018) 250-260.
[27] Q. Lian, G. Deng, A.K. Tieu, H. Li, Z. Liu, X. Wang, H. Zhu, Thermo-mechanical coupled finite element analysis of rolling contact fatigue and wear properties of a rail steel under different slip ratios, Tribology International, 141 (2020) 105943.
[28] Y.C. Chen, S.Y. Lee, Elastic-plastic wheel-rail thermal contact on corrugated rails during wheel braking, Journal of Tribology, (2009).
[29] C. He, Z. Yang, P. Zhang, R. Dollevoet, Z. Li, Thermomechanical finite element modelling of wheel-rail contact and experimental validation, Tribology International, 209 (2025).
[30] C. He, Z. Yang, P. Zhang, S. Li, M. Naeimi, R. Dollevoet, Z. Li, A finite element thermomechanical analysis of the development of wheel polygonal wear, Tribology International, 195 (2024).
[31] V.-G. (n.d.), VI-Rail. Retrieved October 7, 2025, from https://www.vi-grade.com/en/products/vi-rail/.
[32] Stadler GTW 2/8 EMU . Retrieved August 2025, from https://trainspo.com/model/1453/.
[33] E.E. Magel, A survey of wheel/rail friction (No. DOT/FRA/ORD-17/21), United States. Federal Railroad Administration. Office of Research, Development, and Technology., (2017).
[34] B. White, R. Lewis, D. Fletcher, T. Harrison, P. Hubbard, C. Ward, Rail-wheel friction quantification and its variability under lab and field trial conditions, Proceedings of the Institution of Mechanical Engineers, Part F: Journal of Rail and Rapid Transit, 238 (2023) 569-579.
[35] ProRail & Arriva, Final report ATO exploratory study Groningen, Groningen, The Netherlands., (2021).
[36] B. Peng, S. Iwnicki, P. Shackleton, D. Crosbee, Comparison of wear models for simulation of railway wheel polygonization, Wear, 436-437 (2019).
[37] H.E. Boyer, T.L. Gall, Metals handbook; desk edition., (Dec. 1984.).
[38] F. Ren, Z. Yang, Z. Li, Experimental investigation and constitutive modelling of the mechanical and ratcheting properties in rail steels, Intelligent Transportation Infrastructure, 4 (2025).
[39] X. Deng, Z. Qian, Z. Li, R. Dollevoet, Investigation of the formation of corrugation-induced rail squats based on extensive field monitoring, International Journal of Fatigue, 112 (2018) 94-105.
[40] C. He, Z. Li, Analysis of ATO-induced wear, TU Delft report, (14 August 2025).
[41] C. He, P. Zhang, Z. Yang, R. Dollevoet, Z. Li, Infrared temperature measurement of wheel-rail frictional rolling contact with high slip ratios, Case Studies in Thermal Engineering, 73 (2025).
[42] J.J. Kalker, Three-dimensional elastic bodies in rolling contact, Netherlands: Springer, (1990).
[43] G. Hang, C. He, Z. Yang, A parametric study on flat-induced impact responses for wheel condition monitoring, 13th International Conference on Contact Mechanics and Wear of Rail/Wheel Systems, CM2025, Tokyo, Japan, (2025).
[44] S. Iwnicki, J.C.O. Nielsen, G. Tao, Out-of-round railway wheels and polygonisation, Vehicle System Dynamics, 61 (2023) 1787-1830.
[45] C. Bernsteiner, G. Müller, A. Meierhofer, K. Six, D. Künstner, P. Dietmaier, Development of white etching layers on rails: simulations and experiments, Wear, 366-367 (2016) 116-122.
[46] E.E. Magel, Rolling Contact Fatigue: A Comprehensive Review, (2011).
[47] Z. Li, R. Dollevoet, M. Molodova, X. Zhao, Squat growth—Some observations and the validation of numerical predictions, Wear, 271 (2011) 148-157.
[48] Z. Li, Molodova, M., Zhao, X., & Dollevoet, R, Squat treatment by way of minimum action based on early detection to reduce life cycle costs . In Joint Rail Conference (Vol. 49064, pp. 305-311).
[49] A. Smith, S. Iwnicki, A. Kaushal, K. Odolinski, P. Wheat, Estimating the relative cost of track damage mechanisms: combining economic and engineering approaches, Proc Inst Mech Eng F J Rail Rapid Transit, 231 (2017) 620-636.

[50] K. trillingen, WeBoost, report number WBD2021-054, (20 April, 2022).
[51] G. Tao, Z. Wen, X. Jin, X. Yang, Polygonisation of railway wheels: a critical review, Railway Engineering Science, 28 (2020) 317-345.
[52] M. Zhang, Zhang, Q., Lv, Y., Sun, W., & Wang, H., An_AI_based_High-speed_Railway_Automatic_Train_Operation_System_Analysis_and_Design, In 2018 International Conference on Intelligent Rail Transportation (ICIRT) (pp. 1-5). IEEE., (2018).
[53] A. Plissonneau, D. Trentesaux, W. Ben-Messaoud, A. Bekrar, AI-based speed control models for the autonomous train: a literature review, 2021 Third International Conference on Transportation and Smart Technologies (TST), 2021, pp. 9-15.